ISSN 0915-633X

# NATIONAL INSTITUTE FOR FUSION SCIENCE

## A Study of High-Energy Ions Produced by ICRF Heating in LHD

K. Saito, R. Kumazawa, T. Mutoh, T. Seki, T. Watari, T. Yamamoto, Y. Torii, N. Takeuchi C. Zhang, Y. Zhao, A. Fukuyama,
F. Shimpo, G. Nomura, M. Yokota, A. Kato, M. Sasao, M. Isobe, A.V. Krasilnikov, T. Ozaki, M. Osakabe, K. Narihara,
Y. Nagayama, S. Inagaki, K. Itoh, T. Ido, S. Morita, K. Ohkubo, M. Sato, S. Kubo, T. Shimozuma, H. Idei, Y. Yoshimura,
T. Notake, O. Kaneko, Y. Takeiri, Y. Oka, K. Tsumori, K. Ikeda, A. Komori, H. Yamada, H. Funaba, K.Y. Watanabe,
S. Sakakibara, R. Sakamoto, J. Miyazawa, K. Tanaka, B.J. Peterson, N. Ashikawa, S. Murakami, T. Minami, M. Shoji,
S. Ohdachi, S. Yamamoto, H. Suzuki, K. Kawahata, M. Emoto, H. Nakanishi, N. Inoue, N. Ohyabu, Y. Nakamura, S. Masuzaki,
S. Muto, K. Sato, T. Morisaki, M. Yokoyama, T. Watanabe, M. Goto, I. Yamada, K. Ida, T. Tokuzawa, N. Noda, K. Toi,
S. Yamaguchi, K. Akaishi, A. Sagara, K. Nishimura, K. Yamazaki, S. Sudo, Y. Hamada, O. Motojima, M. Fujiwara

(Received - Aug. 22, 2001)

NIFS-712 Sep. 2001

**RESEARCH REPORT**
**NIFS Series**

TOKI, JAPAN

# A STUDY OF HIGH-ENERGY IONS PRODUCED BY ICRF HEATING IN LHD

K. SAITO*, R. KUMAZAWA, T. MUTOH, T. SEKI, T. WATARI, T. YAMAMOTO*,
Y. TORII*, N. TAKEUCHI*, C. ZHANG**, Y. ZHAO**, A. FUKUYAMA***, F. SHIMPO,
G. NOMURA, M. YOKOTA, A. KATO, M. SASAO, M. ISOBE, A.V. KRASILNIKOV****,
T. OZAKI, M. OSAKABE, K. NARIHARA, Y. NAGAYAMA, S. INAGAKI, K. ITOH, T. IDO,
S. MORITA, K. OHKUBO, M. SATO, S. KUBO, T. SHIMOZUMA, H. IDEI, Y. YOSHIMURA,
T. NOTAKE*, O. KANEKO, Y. TAKEIRI, Y. OKA, K. TSUMORI, K. IKEDA, A. KOMORI,
H. YAMADA, H. FUNABA, K.Y. WATANABE, S. SAKAKIBARA, R. SAKAMOTO,
J. MIYAZAWA, K. TANAKA, B.J. PETERSON, N. ASHIKAWA*****, S. MURAKAMI,
T. MINAMI, M. SHOJI, S. OHDACHI, S. YAMAMOTO*, H. SUZUKI, K. KAWAHATA,
M. EMOTO, H. NAKANISHI, N. INOUE, N. OHYABU, Y. NAKAMURA, S. MASUZAKI,
S. MUTO, K. SATO, T. MORISAKI, M. YOKOYAMA, T. WATANABE, M. GOTO,
I. YAMADA, K. IDA, T. TOKUZAWA, N. NODA, K. TOI, S. YAMAGUCHI, K. AKAISHI,
A. SAGARA, K. NISHIMURA, K. YAMAZAKI, S. SUDO, Y. HAMADA, O. MOTOJIMA,
M. FUJIWARA
National Institute for Fusion Science, Toki, Japan.
* Nagoya University, Faculty of Engineering, Nagoya, Japan.
** Academia Sinica Plasma Physics Institute, Hefei, China.
*** Kyoto University, Department of Nuclear Engineering, Kyoto, Japan.
**** Troitsk Institute for Innovating and Fusion Research (TRINITI), Troitsk, Russia.
***** The Graduate University for Advanced Studies, Toki, Japan.

**ABSTRACT.** This paper reports on the behavior of high-energy ions produced by Ion Cyclotron Range of Frequency (ICRF) heating on the Large Helical Device (LHD). In the 3rd experimental campaign conducted in 1999, it was shown that minority heating has high heating efficiency, and high-energy particles were also observed. In the 4th campaign in 2000 the temporal behavior of high-energy ions was investigated in the minority heating regime using turn-off or modulation of ICRF power. The time evolution of the high-energy particle distribution was measured using a natural diamond detector (NDD) and a time-of-flight neutral particle analyzer (TOF-NPA). It was found that the count number of higher-energy particles declines faster than that of lower-energy particles after ICRF turn-off. In the modulation experiments, the phase difference of the flux of high-energy particles with respect to the ICRF power modulation increased with energy. These results were explained qualitatively by the Fokker-Planck equation with a simple model. The pitch-angle dependence of the distribution function was also measured in the experiment by changing the line of sight of the TOF-NPA. An anisotropy of the high-energy tail was found. This anisotropy was reproduced by solving the bounce-averaged Fokker-Planck equation. The second harmonic heating was conducted successfully for the first time during high beta plasma experiments in the LHD. High-energy particles were also detected in this heating regime.

Keywords:
ICRF heating, high-energy ions, power modulation, anisotropy of distribution function, second harmonic heating, LHD

# 1. INTRODUCTION

Ion Cyclotron Range of Frequency (ICRF) heating has been conducted in many tokamaks and several stellarators. In CHS electron heating was demonstrated successfully. In ion heating, however, the plasma could not be sustained due to the increase of radiation power [1]. In W7-AS, various heating regimes such as D(H) minority heating, D,H mode conversion heating, and second harmonic H heating [2] were examined solving impurity problems by use of boronization.

The LHD (Large Helical Device) is a super-conducting helical device with the poloidal and troidal periods of $l$=2 and $m$=10 [3-6]. The major and minor radii are 3.9 m and 0.6 m, respectively. A major goal of this device is to achieve high fusion triple products, high density, high beta, and steady state operation in the helical system with current-less plasmas. The ICRF heating system in the LHD has been developed to conduct high power and long pulse experiments.

ICRF heating was examined in the LHD in the 3rd experimental campaign [7-11] and was shown to be an efficient heating method. The best heating was achieved when the ion cyclotron resonance layer (fundamental of hydrogen) was located near the saddle point [9, 10]. Direct ion heating was dominant in this heating regime, which was deduced from the small change of electron temperature after ICRF injection. High-energy particles were detected in this heating regime. Good confinement of high-energy particles is considered to be the key to the success of ICRF heating [12] and therefore the behavior of high-energy particles was investigated to some extent in the 3rd experimental campaign [13-15]. However, these analyses are mostly based on isotropic treatment of the distribution function in the high-energy part.

In the 4th experimental campaign, conducted in 2000, the behavior of high-energy ions was investigated in more detail by means of studying the dynamic response and pitch-angle dependence of the distribution function in the minority heating. Second harmonic heating was conducted as an advanced alternative to minority heating and the behavior of high-energy ions created by this heating regime was also investigated.

This paper puts emphasis on the understanding of the behavior of high-energy ions created by ICRF heating in the LHD. In section 2, the experimental equipment and the location of resonance and cutoff layers are described. In section 3-1, the behavior of the high-energy ions after the ICRF turn-off is described. In section 3-2 a calculation is introduced to explain this result. In section 3-3, the behavior of the high-energy ions during power modulation is described, and compared with the calculation. In section 4, the anisotropy of the distribution function during ICRF heating is shown, and compared with the calculated result of the bounce-averaged Fokker-Planck equation. In section 5, the results of second harmonic heating are described, and section 6 is a summary.

## 2. EXPERIMENTAL SETUP

Figure 1 is a top view of the LHD, showing the location of heating devices and main diagnostics. Loop antennas [16] have been installed vertically through upper and lower ports. ICRF power is fed from multi-stage amplifiers via impedance matching systems [17] and ceramic feed-throughs. These components are designed to withstand steady state operation [18]. The RF frequency is tunable from 25 to 100 MHz in order to cover various heating regimes: minority heating, mode conversion heating, and higher harmonic heating. The plasma cross-section is vertically elongated in front of the loop antennas. The loop antennas are twisted so as to fit the last closed flux surface (LCFS) of the helical plasma and the Faraday shields are aligned to the magnetic field in order to excite a fast wave. The dimensions of the loop antennas are 46 cm in width, 120 cm in length (the total of the upper and lower antennas), and 17 cm in depth.

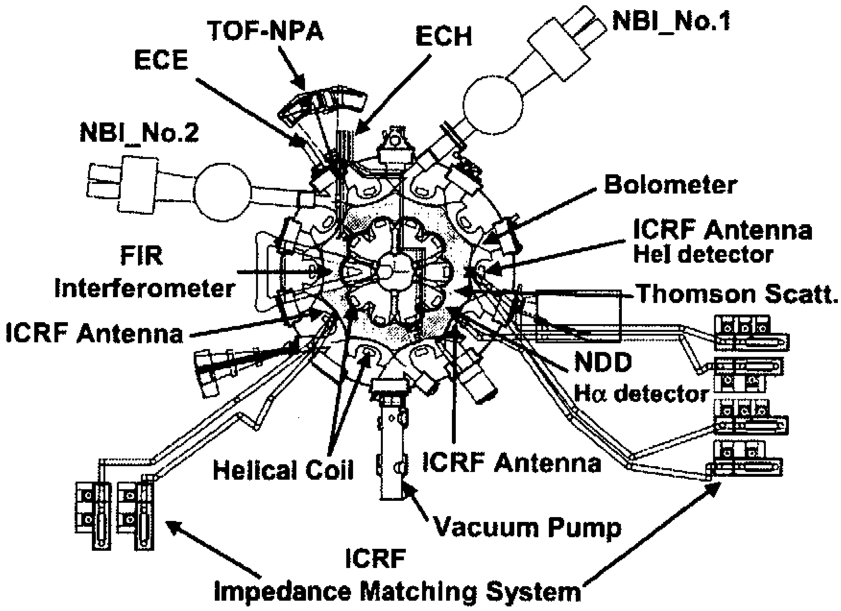

Fig. 1 Top view of the LHD with heating devices and diagnostics.

Initial plasma is produced by electron cyclotron heating (ECH); in some experiments plasma is sustained by ICRF heating only, while in other experiments ICRF heating was superposed on neutral beam injection (NBI) heating.

The main diagnostics are an FIR interferometer, a wide angle bolometer, Thomson scattering, an electron cyclotron emission (ECE) system, Hα/HeI detectors, a natural diamond detector (NDD) [13-15], and a time-of-flight neutral particle analyzer (TOF-NPA) [19]. Both NDD and TOF-NPA detect the high-energy neutral particles which escape out of the plasma via a charge exchange process. The line of sight of the NDD is perpendicular to the plasma column so that the population of ions with almost perpendicular pitch angle (82°-102°) is measured. The TOF-NPA is installed horizontally at the middle plane of the LHD and the line of sight is changeable.

Helium and hydrogen are used as working gas. Figure 2 shows the layers of ion cyclotron resonance (fundamental of hydrogen), ion-ion hybrid resonance, R cut-off, and L cut-off for the RF frequency $f$=38.47 MHz and the magnetic field strength on the magnetic axis $B_0$=2.75 T as a typical case. Here, dielectric constants of the cold-plasma approximation were used. A density profile of $n_e = n_{e0}(1-\rho^8)$ is assumed in the calculation of Fig. 2, where $\rho$ is the normalized minor radius and $n_{e0} = 1.0 \times 10^{19}$ m$^{-3}$ is the electron density on the magnetic axis. The minority ion ratio $n_H/(n_H + n_{He}) = 5$ % and the wave number parallel to the magnetic line of force $k_{//} = 5$ m$^{-1}$ are used in this calculation.

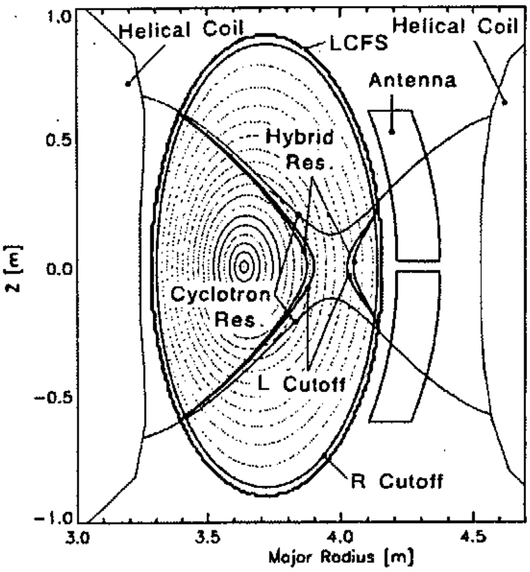

Fig. 2 Location of layers of ion cyclotron resonance, ion-ion hybrid resonance, R cut-off, and L cut-off in front of ICRF antennas for $f$=38.47 MHz and $B_0$=2.75 T. In this calculation $n_{e0} = 1.0 \times 10^{19}$ m$^{-3}$, $n_H/(n_H + n_{He}) = 5\,\%$, and $k_{//} = 5$ m$^{-1}$ were used.

## 3. TEMPORAL BEHAVIOR OF HIGH-ENERGY IONS

In order to understand the mechanism of ICRF heating, the time evolution of the distribution function is studied in this section. We conducted two experiments: 1) The ICRF power was turned off and the following evolution of the high-energy ion tail was measured with the NDD and 2) the ICRF power was modulated and the response of the distribution function was measured with the TOF-NPA. The results of the theoretical calculations are compared with those of the experiments for these two cases.

### 3-1. EVOLUTION OF HIGH-ENERGY ION TAIL AFTER ICRF TURN-OFF

Figure 3-(a) shows the time evolution of an ICRF heating discharge. NBI was added from $t$=1.3 sec. In this discharge the magnetic field strength on the axis was $B_0$=2.8 T, and two pulses of RF frequencies $f$=38.47 MHz ($t$=0.4-2.5 sec) and 40.47 MHz ($t$=2.0-2.5 sec) were applied. The electron density was

measured with a 13-channel FIR interferometer, the electron temperature was measured with a Thomson scattering measurement, and the radiation power was measured with a wide angle bolometer. The bottom figure is the count number of neutral particles detected with the NDD.

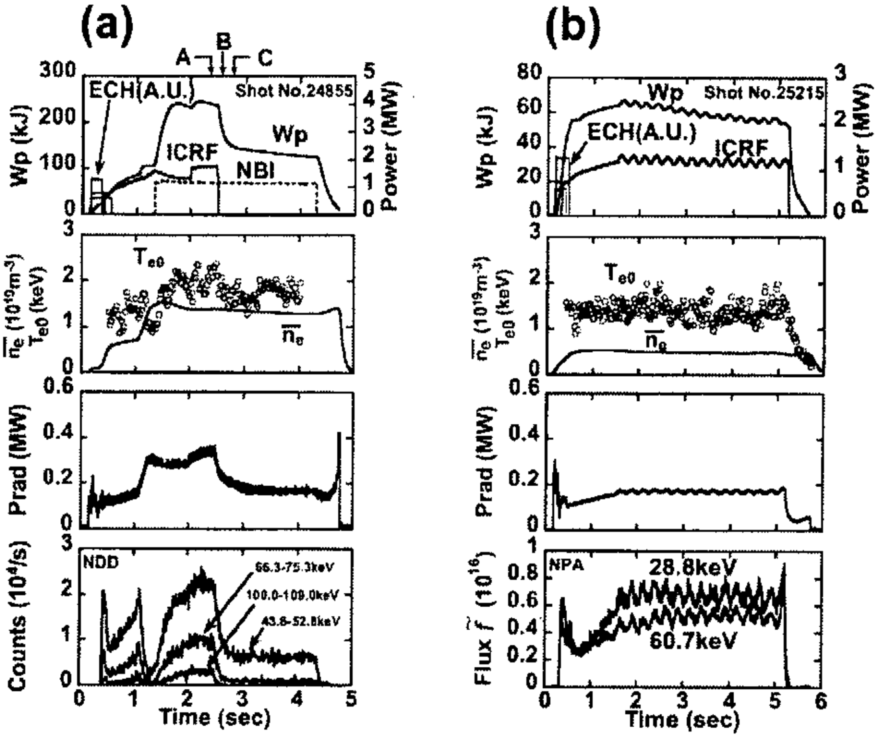

Fig. 3 The dynamic responses of the plasma to the ICRF power:

(a) The time evolution of plasma parameters as the power is turned off. The ICRF power is turned off at $t$=2.5 sec.

(b) The time evolution of plasma parameters in the power modulation experiment. The ICRF power is modulated and the flux of high-energy particles is also modulated. The flux $\tilde{f}$ is defined by $\delta N = (4\pi)^{-1}\sqrt{E}\,\tilde{f}\,\delta\Omega\,\delta E\,\delta t$ with measured count number $\delta N$. Here, $\delta\Omega$ is the solid angle of the aperture of the detector. $E$ and $t$ are measured in keV and sec, respectively.

Figure 4 shows the ion energy distribution in the discharge of Fig. 3-(a) as observed by the NDD. The ordinate is the direct count number of neutral particles for 0.1 sec. In this figure, the labels A to C with arrows indicate the times of measurement shown in Fig. 3-(a) by arrows. The range below 30 keV is affected by the thermal noise of the preamplifier. Count numbers decline after turn-off of ICRF ($t$=2.5 sec).

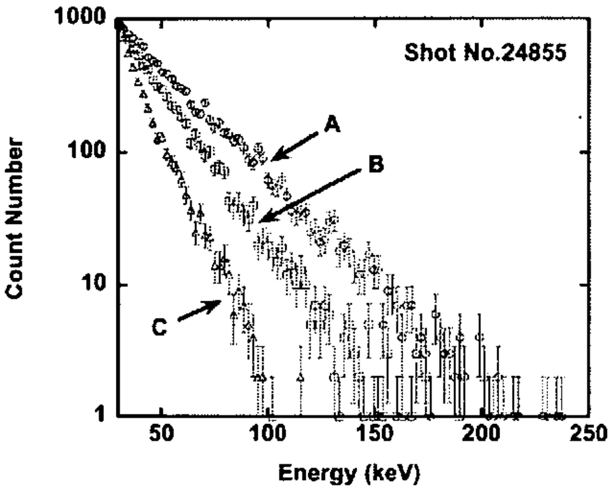

Fig. 4 Temporal change of the ion energy distribution in the discharge of Fig. 3-(a). NDD is used for measurement. The labels A to C denote the times of measurement shown in Fig. 3-(a) by arrows. Count number declines after turn-off of the ICRF heating ($t$=2.5 sec).

Figure 5-(a) shows the time evolution of count numbers of neutral particles detected with the NDD. The count numbers are normalized to the values before turn-off and the background associated with NBI is subtracted so that they are unity at $t$=2.4 sec and zero at $t$=3.0 sec. It was found that particles with high energy decay faster than those with low energy.

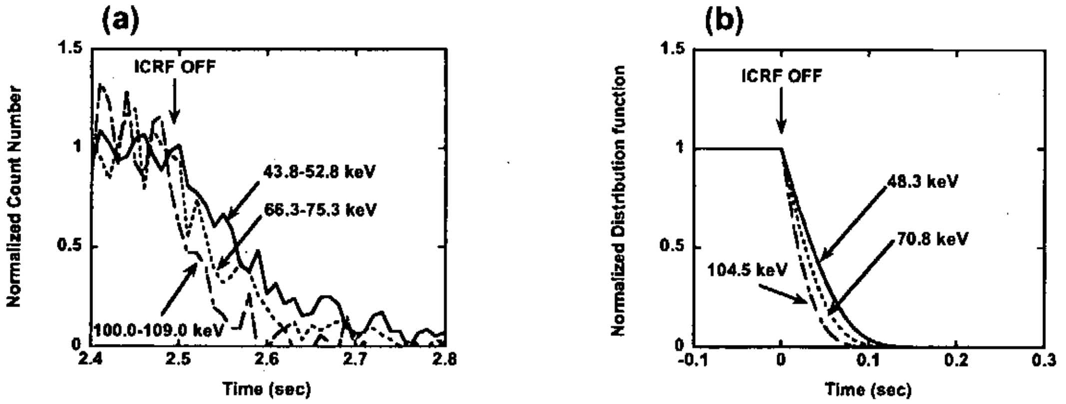

Fig. 5 The decay of high energy particles compared to the theoretical prediction.

(a) Time evolution of the count number of neutral particles measured in the shot shown in Fig. 3-(a). The count numbers are normalized so that they are unity before turn-off and zero at $t$=3.0 sec.

(b) Time evolution of the calculated distribution function in the perpendicular direction.

## 3-2. CALCULATION OF FOKKER-PLANCK EQUATION

A simulation was made using a simple model to understand the experimental results of section 3-1. The distribution function was expanded to the second order in the Legendre polynomials of cos$\Theta$, where $\Theta$ is pitch angle [20],

$$f(v,\Theta,t) = A(v,t) + \frac{1}{2}B(v,t)(3\cos^2\Theta - 1) \tag{1}$$

$A(v,t)$ and $B(v,t)$ are calculated by solving the Fokker-Planck equation in each flux surface:

$$\frac{\partial A}{\partial t} = \frac{1}{v^2}\frac{\partial}{\partial v}\{-\alpha v^2 A + \frac{1}{2}\frac{\partial}{\partial v}(\beta v^2 A) + Kv\frac{\partial}{\partial v}v(A - \frac{B}{5}) - K(A + \frac{2}{5}B)v\} \tag{2}$$

$$\begin{aligned}\frac{\partial B}{\partial t} &= -\frac{1}{v^2}\frac{\partial}{\partial v}(\alpha v^2 B) + \frac{1}{2v^2}\frac{\partial^2}{\partial v^2}(\beta v^2 B) - \frac{3}{2}\frac{\gamma}{v^2}B \\ &\quad + \frac{K}{v^2}\frac{\partial}{\partial v}v\frac{\partial}{\partial v}v(-A + \frac{5}{7}B) - \frac{K}{v^2}(3A + \frac{30}{7}B) + \frac{K}{v^2}\frac{\partial}{\partial v}v(4A - \frac{5}{7}B)\end{aligned} \tag{3}$$

where,

$$K = \frac{\langle P\rangle}{3n_{\mathrm{H}}m_{\mathrm{H}}},\quad \alpha = \langle\Delta v_{/\!/}\rangle + \frac{1}{2v}\langle(\Delta v_{\perp})^2\rangle,\quad \beta = \langle(\Delta v_{/\!/})^2\rangle, \text{ and }\quad \gamma = \langle(\Delta v_{\perp})^2\rangle$$

$\langle P\rangle$ is averaged absorbed power per unit volume. $\langle\Delta v_{/\!/}\rangle$, $\langle(\Delta v_{/\!/})^2\rangle$, and $\langle(\Delta v_{\perp})^2\rangle$ are the Coulomb diffusion coefficients. In this model the effect of anisotropy is included to the extent that it is reflected in the second term in Eq. (1). Drift motion crossing flux surfaces is ignored in this model and the distribution function is assumed to be uniform on a flux surface.

The calculation was made with the plasma parameter relevant to the shot shown in Fig. 3-(a): A normalized minor radius of $\rho$=0.5 is taken since power deposition is largest there [10]. The electron density $n_e$ is $1.3\times10^{19}$ m$^{-3}$ on this flux surface and almost constant in time. ECE data were used to obtain variation of the electron temperature, $T_e = 0.3\exp\{-(t-2.5)/0.1\} + 1.3$ keV. The ECE signal was calibrated against the Thomson scattering measurement. The temperature of helium was assumed to be same as the electron temperature because bulk ions couple strongly with electrons. The hydrogen density, $n_{\mathrm{H}}$ was estimated to be $5.4\times10^{17}$ m$^{-3}$ from the ratio of Hα signal to HeI [10]. In this calculation parameter $K$ was adjusted to $1.3\times10^{13}$ W/kg so that the experimental effective temperature $T_{\mathrm{eff}}$=29 keV in the energy range around 130 keV is obtained. These values are used in the calculation of Eqs. (2) and (3). Figure 5-(b) shows the calculated time evolution of the normalized distribution function in the perpendicular direction, $\Theta$=90°. The distribution function decays slowly in the lower energy range because higher energy particles drop to this lower energy region. This tendency agrees with the experimental result qualitatively.

### 3-3. POWER MODULATION EXPERIMENT

Power modulation experiments were also conducted in order to understand the behavior of high-energy ions. The magnetic field strength on the axis is $B_0$=2.75 T, and the RF frequency is $f$=38.47 MHz. The

ICRF power was modulated sinusoidally at a frequency of 4 Hz with an amplitude of 80 kW. Figure 3-(b) shows the time history of the plasma parameters of a typical shot. The electron temperature on the magnetic axis was $T_{e0}$=1.4 keV on time average and the line-averaged electron density was constant, $\overline{n_e}$ =0.5×10$^{19}$ m$^{-3}$ during the power modulation. The plasma stored energy shows a clear response to the modulated power as shown in the first column. The radiated power shown in the third column and the flux of neutral particles shown in the fourth column are also modulated. The latter was measured with the TOF-NPA, where the angle of the line of sight with respect to the magnetic axis was $\phi$=73.3°.

It is found that the flux is to a certain degree out of phase with the modulated ICRF power and the phase difference is larger in higher energies. A Fourier analysis was made to determine the small phase difference accurately. The solid circles in Fig. 6-(a) show the experimentally obtained phase delay of the modulation of the flux relative to the ICRF power, plotted against the energy of the particles. The solid circles in Fig. 6-(b) show the amplitude of the modulation of the flux.

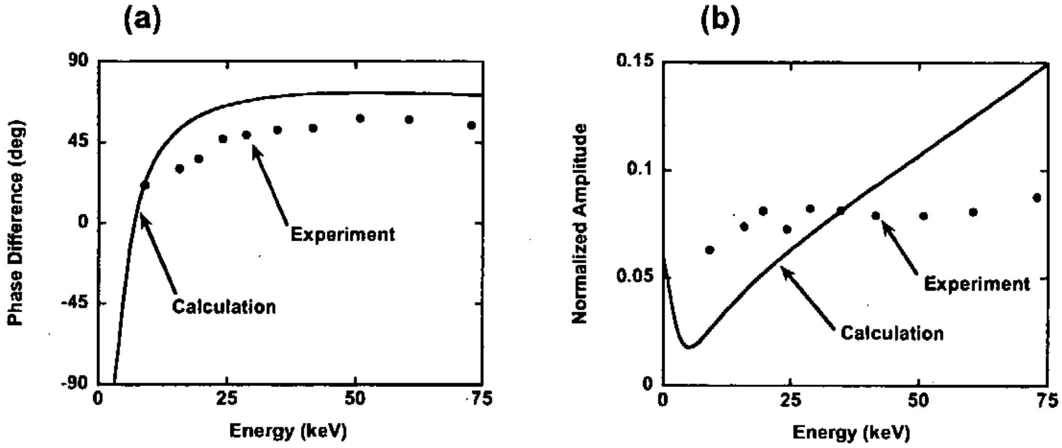

Fig. 6 The dependence of the response of high-energy particles on their energy to the power modulation.

(a) Phase difference of count number relative to the ICRF injected power. Solid circles represent the experimental result measured with the TOF-NPA. The solid line shows the result of simulation.

(b) Normalized amplitude of count number. Solid circles represent the experimental result. The ordinate is the amplitude of the modulation of the flux normalized to its time average. The solid line shows the result of simulation.

The analysis described in section 3-2 is adapted to the modulation experiment by writing $K$ as:

$$K = \overline{K} + \Delta K \sin \omega t \tag{4}$$

Here, $\overline{K}$, $\Delta K$, and $\omega$ are the mean RF power, the amplitude of modulation, and the modulation frequency, respectively. A simulation was made with respect to the shot shown in Fig. 3-(b) specifying the flux surface. $\rho$=0.75 was chosen for a reason that will be mentioned in section 4. An experimental value of $n_e$=0.4×10$^{19}$ m$^{-3}$ was used for the plasma density. The hydrogen concentration $n_H$ was estimated to be $4\times10^{17}$ m$^{-3}$. Electron and helium temperatures were also assumed to be constant at $T_e=T_{He}=0.7$ keV because the ECE signal was almost constant. Figure 7 shows the calculated time evolution of the distribution function. Though the distribution function is obtained as a function of velocity $v$ and pitch angle $\Theta$, we set $\Theta=73.3°$ because direct comparison with the experiment can be made only at this pitch angle. The ordinates of the traces in Fig. 7 are, therefore, $f=f(v, \Theta=73.3°, t)$. The top column in Fig. 7 is the modulated power given by Eq. (4) as a reference. From the second to the sixth columns, the behavior of the distribution function at various energies is shown. They show sinusoidal oscillation with phase and amplitude depending on the energy. It is found that the phase difference increases with energy. It is noteworthy to point out that the distribution function of particles with lower energy oscillates with reverse sign with respect to that of high-energy particles. This suggests conservation of particles in velocity space. The amplitude of the oscillation depends on the energy of the particles with a minimum at around 10 keV. Calculations show such energy is dependent on the input power, becoming higher with increasing power. The solid line in Fig. 6-(a) shows the calculated phase difference against the energy of the particles. It is noted that $\overline{K}$ is a free parameter in solving the set of equations (1) to (3), while the ratio $\Delta K$ to $\overline{K}$ is taken from the experiment ($\Delta K/\overline{K}=6.5$ %). The best fit with the experiment was obtained with $\overline{K}=0.5\times10^{13}$ W/kg. This value is reasonable since it gives an effective temperature of 11 keV in the energy range around 50 keV, which is close to the experimentally obtained value measured with NDD. The solid line in Fig. 6-(b) shows the calculated amplitude of the modulation against the energy of the particles, compared with the experimental amplitudes shown by the solid circles. The simulation results explain well the tendency for the amplitude to increase with energy in the experimental range of energy. However, the simulation shows a larger dependence on the energy in the high-energy region than that obtained in the experiment. Elaborations of both the theory and the experiment are necessary in order to obtain full agreement between them.

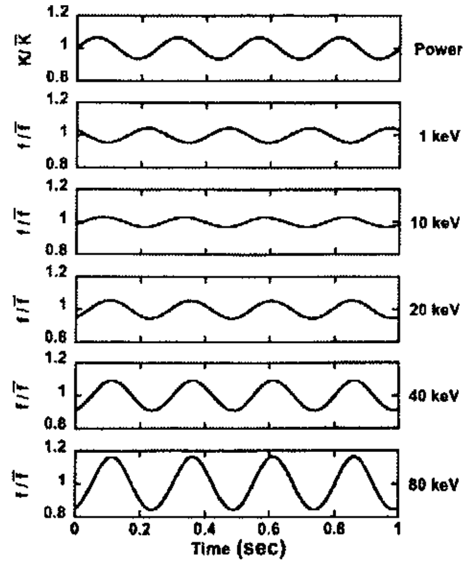

Fig. 7 Time evolution of the modulated power and the distribution function calculated with the parameters of Fig. 3-(b). The ordinates are the distribution functions at various particle energies normalized to their time average $\overline{f}$. On the top, $K/\overline{K}$ is shown for reference.

## 4. ANISOTROPY OF DISTRIBUTION FUNCTION

Ions are trapped as they are heated by ICRF in the perpendicular direction and they become unable to cross the cyclotron resonance layer since they reflect before they reach the layer. It is known in tokamak experiments that the distribution function of ICRF heated plasma is, thus, unique, a phenomenon which is not expressed by the two-term approximation in the previous section. In order to investigate how such an effect is reflected in ICRF heating in helical systems, the dependence of the distribution function on pitch angle was studied by use of the TOF-NPA.

The angle of the line of sight with respect to the magnetic axis, $\phi$, was scanned from 40.4° to 93.9° shot by shot using five successive discharges sustained by ICRF in the minority heating regime. Plasma parameters and ICRF injection power were kept constant: $\overline{n}_e = 0.9\times10^{19}\ \mathrm{m}^{-3}$, $T_{e0}$=1.5 keV, and $P_{\mathrm{ICRF}}$=1.45 MW. Figure 8 shows the contour of flux of neutral particles shown in polar coordinate with $\phi$ the angle and $\sqrt{2E/m_{\mathrm{H}}}$ the modulus, where $E$ is particle energy. The labels $v_{//} = \sqrt{2E/m_{\mathrm{H}}}\cos\phi$ and $v_{\perp} = \sqrt{2E/m_{\mathrm{H}}}\sin\phi$ on the abscissa and ordinate are nominal, signifying parallel and perpendicular velocity on the magnetic axis only. In order to compensate for the difference of the viewing volume, which depends on the line of sight, fluxes are normalized on an assumption that the distribution function was isotropic at the energy range of 6 keV. It was found that the flux of neutral particles is largest at the angle of $\phi \cong 70°$. This may be related to a so-called "butterfly" ("rabbit-ear") structure of the distribution function [21-24].

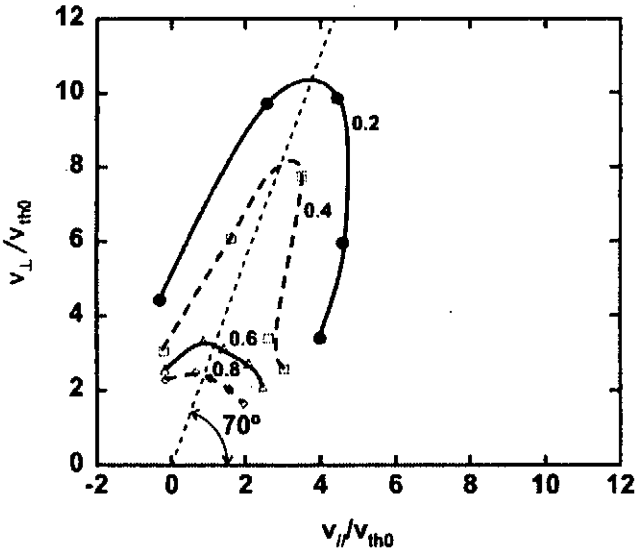

Fig. 8 Contour of count number of neutral particles detected with the TOF-NPA. The contour of the count number is shown in a polar coordinate ($\phi$, $\sqrt{2E/m_{\mathrm{H}}}$ ). The direction of the line of sight is scanned in five successive shots keeping plasma parameters and ICRF injection power constant.

The particles are accelerated perpendicularly to the magnetic line of force near the cyclotron resonance layer increasing the population of trapped particles. The particles stop being accelerated when they are trapped deeply so that the banana orbits no longer cross the ion cyclotron resonance layer. Therefore, the particles with a pitch angle of 90° have the largest population near the ion cyclotron resonance layer. The peak of the modulation will be shifted to a lower angle as they are observed at the bottom of the magnetic field, creating the "butterfly" structure.

Due to the conservation of energy and magnetic moment, the pitch angle $\Theta$ of the particles that are mirror-reflected just on the ion cyclotron resonance layer is related to the local magnetic field strength $B$ by the following equation:

$$\sin^2\Theta = B / B_{res} \tag{5}$$

Here, $B_{res}$ is the magnetic field strength on the ion cyclotron resonance layer (2.52 T). $B$ is a function of $\phi$ and $L$, the angle of the line of sight and the length from the pivot point of the TOF-NPA, respectively:

$$B = B(\phi, L) \tag{6}$$

The pitch angle of a particle, $\Theta$, which is identically the angle between the magnetic line of force and the line of sight, is also a function of $\phi$ and $L$:

$$\Theta = \Theta(\phi, L) \tag{7}$$

By solving the set of equations (5)-(7) numerically, $L$ is obtained as a function of $\phi$. Specifically, for $\phi$ =70°, $L$ is determined to be 2.66 m. The point $(L, \phi)$=(2.66 m, 70°) corresponds to $(\rho, \theta, \varphi)$= (0.75, 0°, 16.5°) in the toroidal coordinate of the LHD. Here, $\rho$ is the normalized minor radius, $\theta$ is the poloidal angle, and $\varphi$ is the toroidal angle. $\theta$=0°, for the line of sight is on the equatorial plane. The position is close to the minimum $B$ along the magnetic lines of force, for the plasma is horizontally elongated at $\varphi$=18°. The experimental result suggests that the strongest wave particle interaction occurs around the flux surface, $\rho$=0.75. This value is close to the predicted value $\rho$= 0.5 in the previous analysis of the power deposition profile. The remaining difference may be understood by considering the population of the neutral particles, which increases with increasing $\rho$.

We employ $\rho$=0.75 in the following calculation of the distribution function. The simple model mentioned in section 3-2 cannot apply to the "butterfly" structure of the distribution function. Therefore, we solve the bounce-averaged Fokker-Planck equation [21-24], the time span considered here being longer than the bounce period, $\tau_b$:

$$\frac{\partial f_0}{\partial t} = \frac{1}{\tau_b} \int \frac{dl}{v_{//}} [C(f_0) + Q(f_0)] \tag{8}$$

The distribution function $f_0$ is thus independent of $l$, the length along the magnetic line of force. The collision term, $C(f_0)$, and the quasi-linear diffusion term for cyclotron absorption, $Q(f_0)$ are averaged along the magnetic lines of force weighted by $1/v_{//}$. Figure 9 shows contour lines of a calculated steady state distribution function in the velocity space at $(\rho, \theta, \varphi)$=(0.75, 0°, 18°) where the magnetic field is at the bottom. The particles on the solid lines have banana tips on the ion cyclotron resonance layer. The dashed lines show the boundary between passing and trapped particles, above which particles are trapped. It is seen that a large fraction of the particles are in the trapped region and the particles whose banana tips are near the ion cyclotron resonance layer have the largest population; i.e., the "Butterfly" structure of the distribution function is manifested. The particles whose pitch angles are 90° cannot cross the ion cyclotron resonance layer, but the number of them increases due to pitch angle scattering. In the calculation of $Q(f_0)$, the left hand component of the RF electric field is deduced from the elements of the dielectric tensor, assuming a uniform RF electric field strength of 10 kV/m in the propagating region. In the evanescent region, the electric field is put zero. Allowing the fast wave of various $k_{//}$, $Q(f_0)$ is integrated over the calculated $k_{//}$ spectrum. The algorism solving the Fokker-Planck equation is similar to the one used in tokamaks, and the only difference is in the bounce-average. While magnetic field has only toroidal ripple in tokamaks, both toroidal and helical ripples have to be considered in helical systems. The magnetic field is obtained by solving the Biot-Savart equation. The boundary of trapped and passing particles shown by the dashed lines in Fig. 9 is thus associated with the reflection of particles at the maximum $B$ including both toroidal and helical ripple.

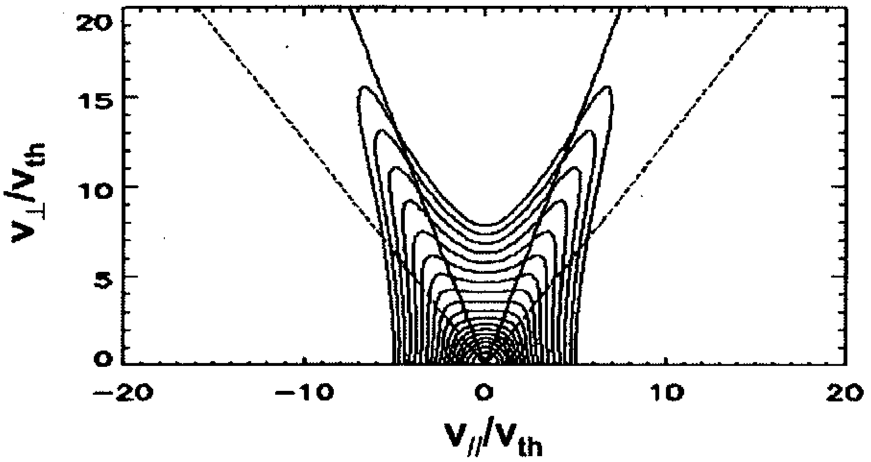

Fig. 9 Contour of the calculated distribution function by solving the bounce-averaged Fokker-Planck equation. $V_{//}$ and $V_\perp$ on the axes are normalized to $V_{th}$, the thermal velocity of hydrogen calculated with $T_H$=0.75 keV at $\rho$=0.75.

## 5. SECOND HARMONIC ICRF HEATING EXPERIMENTS

It is known that second harmonic heating is due to the finite Larmor radius effect and, therefore, high-energy ions are accelerated preferentially creating a high-energy tail. It is thus assumed necessary to have good confinement of high-energy particles in order to have a good heating performance. The viability of second harmonic heating was established in tokamaks back in the 1980's and it is regarded as a reliable heating scheme [25, 26]. However, it was only recently that ICRF heating was demonstrated to be viable in helical systems [1, 2, 7-11]. In the experiment in W7-AS, second harmonic heating was examined with other various heating regimes. It is reported that about 70% of the ICRF power was absorbed in plasma in W7-AS [2] even though second harmonic damping is known to be a weak absorption mechanism.

In the LHD a second harmonic ICRF heating experiment was conducted in the 4th experimental campaign by lowering the magnetic field strength and clear heating was obtained for the first time. Figure 10 shows a discharge with second harmonic heating superposed on an NBI target plasma. The magnetic field strength on the axis was $B_0$=1.363 T. Two pulses with frequencies $f$=38.47MHz and 40.47 MHz were applied from $t$=1.0 sec. The former had a pulse length of 0.6 sec and the latter one of 0.3 sec, and the total injected power was 2 MW in the early 0.3 sec. The difference of the frequency may not be important in this experiment. The plasma stored energy, $W_p$ increased from 110 kJ to 130 kJ at $t$=1.1 sec, a little after RF was turned on, and decreased twice as the ICRF power decreased stepwise. The operational plasma parameters were $\overline{n}_e$ =0.75-1.0×$10^{19}$ $m^{-3}$ and $T_{e0}$ =1.0-1.4 keV. The line-averaged electron density, $\overline{n}_e$ decreased gradually because the gas-puff was switched off at $t$=1.0 sec. Radiation loss increased from 0.3 to 0.5 MW on the application of ICRF, however it saturated in time and the increment of the radiation loss remained 10 % of the injected ICRF power. The electron temperature did not show rapid rise as observed in $W_p$, suggesting that the wave is absorbed mainly by ions.

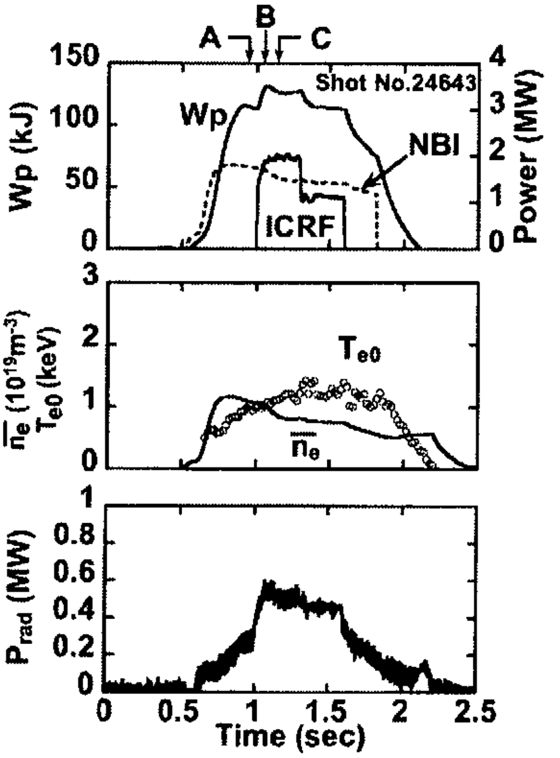

Fig. 10 Discharge with second harmonic ICRF heating superposed on a NBI target plasma. The gas-puff is turned off at $t$=1.0 sec followed by the gradual decay of plasma density.

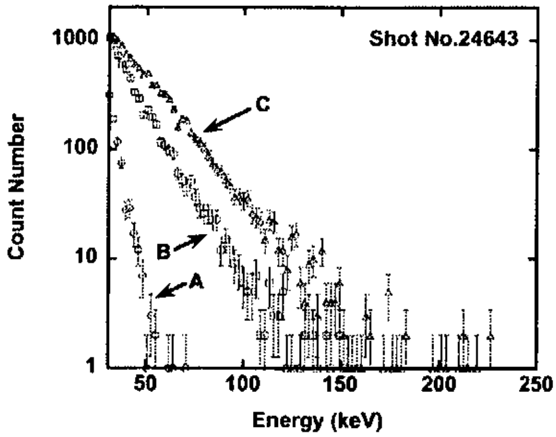

Fig. 11 Energy distribution of neutral particles in the second harmonic heating. The labels A, B, and C designate the time of measurement corresponding to those in Fig. 10. NDD is used for measurement.

Figure 11 shows the energy spectrum of the fast neutrals measured with the NDD. The labels A, B, and C in Fig. 11 correspond to same labels in Fig. 10 showing the time when data were taken. No high-energy tail is observed before RF is applied as shown by A. A high-energy tail is created on the application of RF (B) and it grows as time passes (C). The effective temperature reached 19 keV at time C as it is determined in the energy range around 50 keV. Figure 12 shows the heating efficiency, which is defined as the absorbed power divided by injected ICRF power. The absorbed power was estimated by the change of slope of $W_p$ at the time of turn-off of the RF pulses ($t$=1.3 and 1.6 sec). The abscissa is the magnetic field strength on the magnetic axis. Frequencies were $f$=38.47MHz and 40.47 MHz for the second harmonic heating and $f$=38.47MHz for the minority heating. As shown in this figure the second harmonic heating experiments were conducted with about one half the magnetic field strength of the minority heating. The heating efficiency of second harmonic ICRF heating reached 40 %, however, it was lower than that of the minority heating, and plasma could not be sustained with ICRF heating only, due to weak absorption. Figure 13 shows the beta value dependence of the heating efficiency. Data points are grouped by the magnetic field strength. It was found that the heating efficiency increases with beta value. This tendency is interpreted in terms of enhanced power absorption in high beta plasmas since higher harmonic heating is associated with the finite Larmor radius effect. Therefore, it is expected that the performance will be further improved in future experiments with increasing beta values. Though runaway features are often predicted for second harmonic heating, no special deformation of the tail from the straight line is found in Fig. 11. The injection power may not be sufficient to create runaway ions.

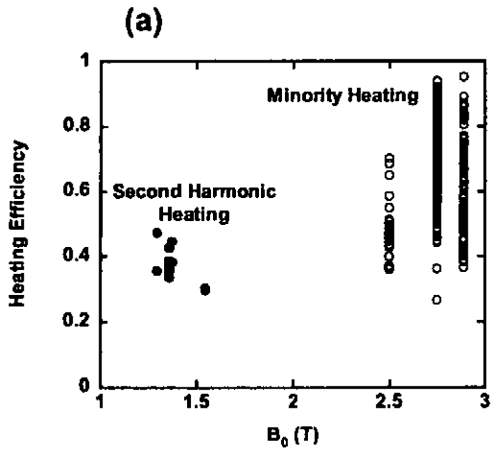

Fig. 12 The dependence of heating efficiency on the magnetic field strength. A peak of the efficiency is found at $B$=2.75 T corresponding to the fundamental heating. The other peak is found at around $B$=1.35 T about half of the former corresponding to second harmonic heating.

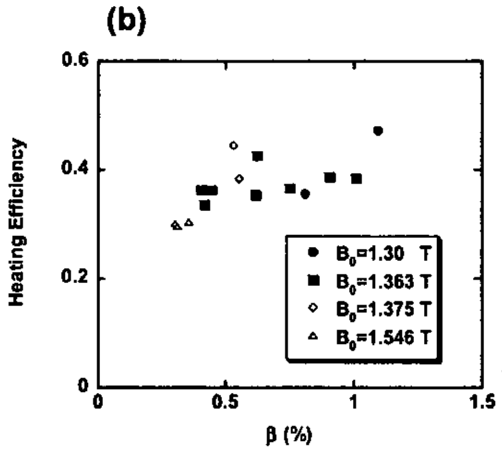

Fig. 13 Heating efficiency versus beta value. There is a tendency that heating efficiency increases with beta value.

## 6. SUMMARY

In order to understand the mechanism of ICRF heating a series of experiments were carried out with emphasis on the behavior of high-energy particles. The temporal behavior of high-energy ions was studied by using the decaying plasma after ICRF turn-off and by using the ICRF power modulation method. The number of particles with higher energy declines faster than that of lower energy ions after ICRF turn-off. In the modulation experiments, phase difference and normalized amplitude increased with energy. These experimental results were explained in terms of the Fokker-Planck equation. Particularly, some of the unique features of the response of the particles are associated with the particle flow in the velocity space.

With respect to the anisotropy of the distribution function, another key subject of ICRF heating reserch, the line of sight of the fast neutral particle analyzer was scanned. The signal had maximum at a certain angle. The result was analyzed by use of the bounce-averaged Fokker-Planck equation and associated with the "butterfly" ("rabbit-ear") structure of the distribution function. In this calculation, the Fokker-Planck equation was modified by means of bounce-average in order to adapt to the helical system.

A second harmonic heating experiment was conducted successfully for the first time in the LHD with an effective temperature of 19 keV. The heating efficiency increases with beta value. This result is consistent with the finite Larmor radius effect on which the heating regime relies. However, a runaway feature expected for this heating regime was not observed within the experimental power range.

### Acknowledgements

The authors wish to thank the technical staff of the LHD group in the National Institute for Fusion Science for their helpful support during this work.

### References

[1] MASUDA, S., et al., Nucl. Fusion **37** (1997) 53.

[2] HARTMANN, D.A., et al., Fusion Energy 1998, vol.2, p575, C&S Papers Series 1/p (1999).

[3] MOTOJIMA, O., et al., Fusion Engineering and Design **20** (1993) 3.

[4] IIYOSHI, A., and YAMAZAKI, K., Physics of Plasmas **2** (1995) 2349.

[5] FUJIWARA, M., et al., Journal of Fusion Energy **15** (1996) 7.

[6] MOTOJIMA, O., et. al., IAEA Conference, 1998, Yokohama, IAEA-CN-69/ FT2/1, "PROGRESS SUMMARY OF LHD ENGINEERING DESIGN AND CONSTRUCTION"

[7] KUMAZAWA, R., et al., Journal of Plasma and Fusion Research SERIES **3** (2000) 352.

[8] WATARI, T., et. al., Nucl. Fusion **41** (2001) 325.

[9] MUTOH, T., et al., Phys. Rev. Let. **85** (2000) 4530.

[10] SAITO, K., et al., Nucl. Fusion **41** (2001) 1021.

[11] KUMAZAWA, R., et al., Physics of Plasmas **8** (2001) 2139.

[12] WATARI, T., Plasma Physics and Controlled Fusion **40** (1998) 13.

[13] SASAO, M., et al., IAEA Conference, 2000, Sorento, IAEA-CN-/EX9/1, "STUDY OF ENERGETIC ION TRANSPORT IN THE LARGE HELICAL DEVICE"

[14] ISOBE, M., et al., Review of Scientific Instruments **72** (2001) 611.

[15] KRASILNIKOV, A.V., et al., submitted to Nucl. Fusion. "ACCELERATION AND CONFINEMENT OF FAST RESONANT PROTONS DURING ICRF AND NBI HEATING IN LHD"

[16] MUTOH, T., et al., Proc. of 14th Symp. on Fusion Engineering **1** (1992) 103.

[17] SAITO, K., et al., Review of Scientific Instruments **72** (2001) 2015.

[18] SEKI, T., et al., Journal of Plasma and Fusion Research SERIES **3** (2000) 359.

[19] OZAKI, T., et al., Review of Scientific Instruments **71** (2000) 2698.

[20] STIX, T.H., Nucl. Fusion **15** (1975) 737.

[21] KERBEL, G.D., and McCOY, M.G., Phys. Fluids **28** (1985) 3629.

[22] CHANG, C.S., and COLESTOCK, P., Phys. Fluids **B2** (1990) 310.

[23] STIX, T.H., WAVES IN PLASMAS, AIP, (1992), p521

[24] CHANG, C.S., Proceedings of the Asian Science Seminar, FRONTIER OF PHYSICS IN FUSION-RELEVANT PLASMAS, p275 (1998).

[25] KIMURA, H., et al., Plasma Physics and Controlled Fusion **35** (1993) 845.

[26] ROGERS, J.H., et al., Fusion Energy 1996, vol.3, p317 (1997).

# Recent Issues of NIFS Series

| | |
|---|---|
| NIFS-686 | S. Toda and K. Itoh,<br>Analysis of Structure and Transition of Radial Electric Field in Helical Systems : Mar. 2001 |
| NIFS-687 | T. Kuroda and H. Sugama,<br>Effects of Multiple-Helicity Fields on Ion Temperature Gradient Modes: Apr. 2001 |
| NIFS-688 | M. Tanaka,<br>The Origins of Elctrical Resistivity in Magnetic Reconnection: Studies by 2D and 3D Macro Particle Simulations: Apr. 2001 |
| NIFS-689 | A. Maluckov, N. Nakajima, M. Okamoto, S. Murakami and R. Kanno,<br>Statistical Properties of the Neoclassical Radial Diffusion in a Tokamak Equilibrium: Apr. 2001 |
| NIFS-690 | Y. Matsumoto, T. Nagaura, Y. Itoh, S-I .Oikawa and T. Watanabe,<br>LHD Type Proton-Boron Reactor and the Control of its Peripheral Potential Structure: Apr. 2001 |
| NIFS-691 | A. Yoshizawa, S.-I. Itoh, K. Itoh and N. Yokoi,<br>Turbulence Theories and Modelling of Fluids and Plasmas: Apr. 2001 |
| NIFS-692 | K. Ichiguchi, T. Nishimura, N. Nakajima, M. Okamoto, S.-i. Oikawa, M. Itagaki,<br>Effects of Net Toroidal Current Profile on Mercier Criterion in Heliotron Plasma: Apr. 2001 |
| NIFS-693 | W. Pei, R. Horiuchi and T. Sato,<br>Long Time Scale Evolution of Collisionless Driven Reconnection in a Two-Dimensional Open System: Apr. 2001 |
| NIFS-694 | L.N. Vyachenslavov, K. Tanaka, K. Kawahata,<br>CO2 Laser Diagnostics for Measurements of the Plasma Density Profile and Plasma Density Fluctuations on LHD Apr. 2001 |
| NIFS-695 | T. Ohkawa,<br>Spin Dependent Transport in Magnetically Confined Plasma: May 2001 |
| NIFS-696 | M. Yokoyama, K. Ida, H. Sanuki, K. Itoh, K. Narihara, K. Tanaka, K. Kawahata, N. Ohyabu and LHD experimental group<br>Analysis of Radial Electric Field in LHD towards Improved Confinement: May 2001 |
| NIFS-697 | M. Yokoyama, K. Itoh, S. Okamura, K. Matsuoka, S. -I. Itoh,<br>Maximum-J Capability in a Quasi-Axisymmetric Stellarator: May 2001 |
| NIFS-698 | S-I. Itoh and K. Itoh,<br>Transition in Multiple-scale-lengths Turbulence in Plasmas: May 2001 |
| NIFS-699 | K. Ohi, H. Naitou, Y. Tauchi, O. Fukumasa,<br>Bifurcation in Asymmetric Plasma Divided by a Magnetic Filter: May 2001 |
| NIFS-700 | H. Miura, T. Hayashi and T. Sato,<br>Nonlinear Simulation of Resistive Ballooning Modes in Large Helical Device: June 2001 |
| NIFS-701 | G. Kawahara and S. Kida,<br>A Periodic Motion Embedded in Plane Couette Turbulence: June 2001 |
| NIFS-702 | K. Ohkubo,<br>Hybrid Modes in a Square Corrugated Waveguide: June 2001 |
| NIFS-703 | S.-I. Itoh and K. Itoh,<br>Statistical Theory and Transition in Multiple-scale-lengths Turbulence in Plasmas: June 2001 |
| NIFS-704 | S. Toda and K. Itoh,<br>Theoretical Study of Structure of Electric Field in Helical Toroidal Plasmas: June 2001 |
| NIFS-705 | K. Itoh and S-I. Itoh,<br>Geometry Changes Transient Transport in Plasmas: June 2001 |
| NIFS-706 | M. Tanaka and A. Yu. Grosberg<br>Electrophoresis of Charge Inverted Macroion Complex: Molecular Dynamics Study: July 2001 |
| NIFS-707 | T-H Watanave, H. Sugama and T. Sato<br>A Nondissipative Simulation Method for the Drift Kinetic Equation: July 2001 |
| NIFS-708 | N. Ishihara and S. Kida,<br>Dynamo Mechanism in a Rotating Spherical Shell: Competition between Magnetic Field and Convection Vortices July 2001 |
| NIFS-709 | LHD Experimental Group,<br>Contributions to 28th European Physical Society Conference on Controlled Fusion and Plasma Physics (Madeira Tecnopolo, Funchal, Portugal, 18-22 June 2001) from LHD Experiment: July 2001 |
| NIFS-710 | V.Yu. Sergeev, R.K. Janev, M.J. Rakovic, S. Zou, N. Tamura, K.V. Khlopenkov and S. Sudo<br>Optimization of the Visible CXRS Measurements of TESPEL Diagnostics in LHD; Aug. 2001 |
| NIFS-711 | M. Bacal, M. Nishiura, M. Sasao, M. Wada, M. Hamabe, H. Yamaoka,<br>Effect of Argon Additive in Negative Hydrogen Ion Sources; Aug. 2001 |
| NIFS-712 | K. Saito, R. Kumazawa, T. Mutoh, T. Seki, T. Watari, T. Yamamoto, Y. Torii, N. Takeuchi C. Zhang, Y. Zhao, A. Fukuyama, F. Shimpo, G. Nomura, M. Yokota, A. Kato, M. Sasao, M. Isobe, A.V. Krasilnikov, T. Ozaki, M. Osakabe, K. Narihara, Y. Nagayama, S. Inagaki, K. Itoh, T. Ido, S. Morita, K. Ohkubo, M. Sato, S. Kubo, T. Shimozuma, H. Idei, Y. Yoshimura, T. Notake, O. Kaneko, Y. Takeiri, Y. Oka, K. Tsumori, K. Ikeda, A. Komori, H. Yamada, H. Funaba, K.Y. Watanabe, S. Sakakibara, R. Sakamoto, J. Miyazawa, K. Tanaka, B.J. Peterson, N. Ashikawa, S. Murakami, T. Minami, M. Shoji, S. Ohdachi, S. Yamamoto, H. Suzuki, K. Kawahata, M. Emoto, H. Nakanishi, N. Inoue, N. Ohyabu, Y. Nakamura, S. Masuzaki, S. Muto, K. Sato, T. Morisaki, M. Yokoyama, T. Watanabe, M. Goto, I. Yamada, K. Ida, T. Tokuzawa, N. Noda, K. Toi, S. Yamaguchi, K. Akaishi, A. Sagara, K. Nishimura, K. Yamazaki, S. Sudo, Y. Hamada, O. Motojima, M. Fujiwara,<br>A Study of High-Energy Ions Produced by ICRF Heating in LHD: Sep. 2001 |